Continuous chemical characterization of ultrafine particulate matter (PM$_{0.1}$)

Georgia A. Argyropoulou[1,2], Kalliopi Florou[1], and Spyros N. Pandis[1,2]

[1] Institute of Chemical Engineering Sciences, ICE-HT/FORTH, Patras, 265 04, Greece
[2] Department of Chemical Engineering, University of Patras, Patras, 265 04, Greece
Correspondence to: Spyros N. Pandis (spyros@chemeng.upatras.gr)

Abstract. Ultrafine particles (diameter less than 100 nm) are primary suspects for enhanced negative health effects on humans. Measuring the chemical composition and physical properties of ultrafine particles on-line, continuously, and accurately is particularly challenging because of their typically low mass concentration (PM$_{0.1}$) and susceptibility to interference from larger particles. The few past PM$_{0.1}$ chemical composition measurement studies have used cascade impactors and at least daily temporal resolution. In this study we perform for the first time high temporal measurements of the composition and sources of PM$_{0.1}$ using an aerodynamic aerosol classifier (AAC) to separate PM$_{0.1}$ from larger particles, integrated with other instruments. These include a high-resolution time-of-flight aerosol mass spectrometer (HR-ToF-AMS, for organics, sulfate, nitrate, ammonium, and chloride), a single-particle soot photometer (SP2-XR, for black carbon) and an Xact625i (for elements).

Ambient PM$_{0.1}$ composition measurements were conducted in a suburban area in Greece to test the system. The hourly PM$_{0.1}$ levels varied from 0.4 to 1.5 μg m^{-3}, with an average of 0.7 μg m^{-3}. Most of the PM$_{0.1}$ (45%) was organic aerosol (OA). On average, sulfates contributed 14%, ammonium 7%, nitrate 3%, and black carbon 4% to PM$_{0.1}$. Calcium (Ca) showed a surprising high average contribution to PM$_{0.1}$ (18%). The rest of the detected elements were Fe, K, Zn and Ti, contributing together 7%. Source apportionment analysis showed that most of the PM$_{0.1}$ OA, during this summertime period, was oxygenated OA (90%), with 70% being less oxidized and 20% being more oxidized, while only 10% was fresh hydrocarbon-like OA.

1. Introduction

Ultrafine particles, also known as UFPs, are particles with diameters less than 0.1 μm and they may represent the most harmful fraction of PM$_{2.5}$ (particulate matter with aerodynamic diameter less than 2.5 μm) (Li et al., 2003; Nel et al., 2006; Schraufnagel, 2020). Exposure to UFPs may

32 lead to increased total and respiratory mortality, respiratory and neurological diseases, and
33 inflammatory markers (Baldauf et al., 2016; HEI, 2013; Ohlwein et al., 2019). Studies indicate
34 that UFPs are able to translocate to sensitive organs of the human body (e.g., brain) and access
35 systemic circulation (Donaldson et al., 2001; Schraufnagel, 2020).

36 Several studies have attempted to establish connections between UFP particle number and
37 health outcomes, however reviews by the U.S. EPA. (2019) and HEI (2013) have rendered these
38 efforts inconclusive. This difficulty in drawing definitive conclusions may stem from the limited
39 number of studies addressing long-term exposure to UFPs (Ostro et al., 2015; Weichenthal et al.,
40 2017; Ohlwein et al., 2019) or might be associated with the metric used in previous UFP health
41 research (Giechaskiel et al., 2022; Kittelson et al., 2022). The number, surface, and mass
42 concentration of ultrafine particles vary over short spatial and temporal scales as a result of
43 emissions, nucleation, coagulation, condensation, and evaporation (Kumar et al., 2016). While
44 UFPs contribute significantly to particle number concentration, they have relatively low mass
45 concentration (Seinfeld and Pandis, 2016). Their high surface area per unit mass allows them to
46 adsorb greater amounts of toxic substances, a property that renders them primary suspects for
47 enhanced negative health effects on humans (Kumar et al., 2016; Kwon et al., 2020).

48 The mass concentration of ultrafine particles ($PM_{0.1}$) has been used as health metric by
49 relatively few studies (Kuwayama et al., 2013; Ostro et al., 2015; Yu et al., 2019; Xue et al., 2020a,
50 b). This limited number of studies can largely be attributed to the challenges associated with
51 measuring $PM_{0.1}$ mass, which is more difficult than the measurement of their number concentration
52 (HEI, 2013; Marval and Tronville, 2022). Nonetheless, directing some attention to $PM_{0.1}$ mass
53 concentration is consistent with the gradual shift in focus from TSP (total suspended particles) to
54 PM_{10} (particulate matter of particles with aerodynamic diameter less than 10 μm) to $PM_{2.5}$, to
55 address the increased risks posed by smaller particles (Li et al., 2003; Jalava et al., 2007; Cassee,
56 Flemming et al., 2019).

57 The European Union has implemented a particle number regulation for the emissions of
58 solid particles with diameter larger than 23 nm (N_{23}). This selection of solid N_{23} as a regulatory
59 metric was guided mainly by technical concerns rather than the corresponding health effects
60 (Giechaskiel et al., 2021). Low correlation between $PM_{2.5}$ and $PM_{0.1}$ has been frequently recorded
61 (Halek et al., 2010; Eeftens et al., 2015; De Jesus et al., 2019; Mataras et al., 2024), which means
62 that strategies aimed towards reducing $PM_{2.5}$ may not inherently result in reducing $PM_{0.1}$.

63   UFPs are commonly defined by their number concentrations, although without a standard

64   lower diameter threshold (Kittelson et al., 2022). For $PM_{0.1}$ on the other hand, the challenge lies

65   on the definition of the upper diameter threshold (Kittelson et al., 2022). A definition of $PM_{0.1}$

66   dependent on the aerodynamic diameter of the particles is consistent with the definitions used for

67   larger particles. However, Tronville et al. (2023) argued that this approach is inappropriate for

68   ultrafine particles, as gravity has a negligible effect on smaller particles, and proposed defining

69    $PM_{0.1}$ based on the physical diameter of particles. In the present study, this definition is adopted

70   and $PM_{0.1}$ represents the mass concentration of particulate matter with physical diameter less than

71   0.1 μm. For spherical particles, the physical diameter is directly equivalent to their electrical

72   mobility diameter (Hinds, 1999; DeCarlo et al., 2004).

73   Newly formed particles are introduced into the atmosphere through either primary sources

74   or secondary formation (Seinfeld and Pandis, 2016; Kumar et al., 2016; Abdillah and Wang, 2023).

75   In urban atmosphere typical combustion sources are traffic, domestic biomass burning, residential

76   or commercial cooking, etc. Burning of agricultural waste, forest fires, power plants and other

77   industrial sources are important in regional scales (Kumar et al., 2016; Moreno-Ríos et al., 2022).

78   Secondary particles are the product of the atmospheric chemical conversion of gas-phase

79   pollutants (SO_2, NH_3, volatile and intermediate-volatility organic compounds) to low-volatility

80   products (H_2SO_4, HNO_3, low volatility organics, and ammonium salts), which are then transferred

81   to the particulate phase through either nucleation or condensation (Seinfeld and Pandis, 2016).

82   The sources of ultrafine particle number and mass tend to be significantly different (Yu et

83   al., 2019). UFP number concentration is mainly influenced by nucleation events, which typically

84   occur during high photochemically active periods, when particulate matter concentrations are quite

85   low, and vapors are unable to condense rapidly on pre-existing particles (Zhang et al., 2015;

86   Giechaskiel et al., 2022). In contrast, nucleation is a minor, or even negligible, source for $PM_{0.1}$

87   mass concentration (Zhang et al., 2015; Yu et al., 2019). The main contributors to ultrafine particle

88   mass are the condensation of secondary organic particulate matter and sulfate (Xue et al., 2020a,

89   b).

90   Measuring the chemical composition and physical properties of ultrafine particles

91   continuously and accurately is particularly challenging because of their typically low mass

92   concentrations and the potential for interference from larger particles during measurement. The

93   few past $PM_{0.1}$ chemical composition studies have used some type of cascade impactor

94 (Kuwayama et al., 2013; Ostro et al., 2015; Corsini et al., 2017; Marcias et al., 2018; Yu et al.,

95 2019; Xue et al., 2020a, b; Beauchemin et al., 2021; Phairuang et al., 2022). However, this

96 approach for $PM_{0.1}$ measurement provides low temporal resolution (daily or longer intervals),

97 requires substantial labor, and may yield results influenced by the presence of larger particles that

98 have substantially higher mass.

99   In this study, we propose an approach for the continuous, automatic measurement of $PM_{0.1}$

100 chemical composition, using the aerodynamic aerosol classifier (AAC, Cambustion) adjusted to

101 operate as a low-pass separator, to separate $PM_{0.1}$ from larger particles, followed by instruments

102 that provide continuous chemical composition measurements and/ or mass spectra. The AAC was

103 also coupled with a Scanning Mobility Particle Sizer (SMPS) to provide information about

104 effective density. The system is tested in a pilot field study to obtain insights into the continuous

105 chemical characterization, physical properties and source apportionment of $PM_{0.1}$.

106

107 **2. Experimental approach**

108 **2.1 The AAC as a $PM_{0.1}$ separator**

109 The aerodynamic aerosol classifier (AAC, Cambustion) is designed to transmit practically

110 monodisperse particles of a selected aerodynamic diameter from 25 nm to over 5 μm. This is

111 achieved by directing the inlet polydisperse aerosol though a rotating cylinder, in which particles

112 are subjected to opposing centrifugal and drag forces. The particles of the selected size follow the

113 intended trajectory and exit through the sample outlet (monodisperse flow) (Fig. 1).

114
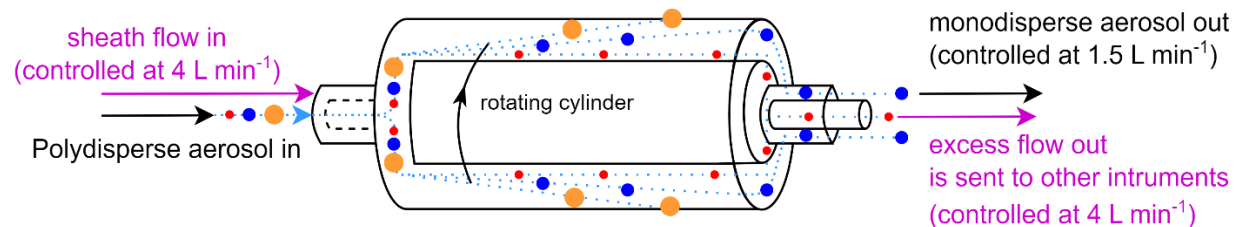
116   **Figure 1. Principle of operation of the AAC when adjusted as a separator.**

117

118 Particles that are larger than the specified size impact the outer wall of the classifier, while particles

119 that are smaller than the specified size exit through the sheath outlet (excess flow). During normal

120 operation, this excess flow, containing the unwanted particles that are smaller than the specified

121 size, is internally filtered and recirculated as sheath flow back into the AAC (Tavakoli and Olfert,
122 2013).

123 The AAC flow system can be adjusted so that the excess flow containing these 'unwanted
124 particles' can be utilized. Instead of recirculating this excess flow back into the AAC, it can be
125 discharged outside the instrument and redirected to other systems (Fig. 1). This modification
126 dilutes the outlet flows (monodisperse flow and excess flow) by a factor equal to the selected
127 (sheath flow in) / (polydisperse flow in) ratio, as the AAC continues to draw filtered clean air
128 through the sheath flow inlet. To ensure proper functionality, the outlet flows must be externally
129 controlled using mass flow controllers (MFC), as this adjustment deviates from the standard
130 operation of the instrument. Accurate size classification and dilution require that the sheath flow
131 in matches the excess flow out, necessitating continuous monitoring of the sheath flow,
132 monodisperse flow, and excess flow. Under these conditions, the AAC operates effectively as a
133 selectable cut-off size separator. In this study, the sheath flow in and the excess flow out were
134 controlled at 4 L min^{-1}, while the polydisperse flow in and monodisperse flow out were maintained
135 at 1.5 L min^{-1}. This configuration optimized the cut-off sharpness and minimized the dilution,
136 resulting in a dilution factor of approximately 2.7.

137 The system was tested using ambient laboratory air to ensure that the dilution and the
138 sharpness of the cut-off are suitable for the typically low PM$_{0.1}$ concentrations, and that there are
139 no significant PM$_{0.1}$ losses within the AAC. The monodisperse flow rate was controlled at 1.5 L
140 min^{-1} with a mass flow controller (MFC; Bronkhorst EL-FLOW Prestige Mass Flow Meter/
141 Controller) before being directed to an exhaust pump (Fig. S1). The excess flow rate was
142 maintained at 4 L min^{-1}. A part of these 4 L min^{-1} equal to 0.6 L min^{-1} was sampled by an SMPS
143 (TSI Classifier model 3080, DMA model 3081, CPC 3775), while the remaining 3.4 L min^{-1} was
144 exhausted through an MFC. A bypass line connected the SMPS to the front of the AAC, allowing
145 the SMPS to alternate sampling between the bypass line and the excess flow line every 30 min
146 over a 2-hour period. The relatively long alternation interval was chosen to verify that the system
147 required minimal time to stabilize the externally controlled flows and achieve a sharp and stable
148 cut-off. Since ambient laboratory air exhibited stable particle concentrations and size distributions,
149 this interval did not affect the accuracy of the results.

150 The mass penetration efficiency of PM$_{0.1}$ was calculated by comparing the average mass
151 size distributions measured by the SMPS between the bypass line and excess flow (Fig. S2). The

152 AAC cut-off (cut diameter where there is 50% mass penetration, d_{50}) was set to an aerodynamic

153 diameter of 140 nm, corresponding to an electrical mobility diameter of 100 nm. For spherical

154 particles, the electrical mobility diameter is equivalent to their physical diameter (Hinds, 1999;

155 DeCarlo et al., 2004). Since $PM_{0.1}$ is defined, in this study, based on the physical particle diameter,

156 the system was calibrated using the electrical mobility diameter as a proxy for the physical

157 diameter d_{50} to be at 100 nm. The mass penetration efficiency at the target d_{50} of 100 nm was

158 approximately 50%, while for particles smaller than 100 nm, it reached 90%. For larger particles,

159 the mass penetration was less than 10% at 120 nm, decreasing to below 5% at 200 nm, and near

160 zero for particles larger than 300 nm. These results demonstrate that the AAC can effectively

161 function as a $PM_{0.1}$ separator at ambient concentrations, with minimal particle losses.

162   A second test was conducted to determine the $PM_{0.1}$ losses when the AAC outlet flows

163 (monodisperse flow and excess flow) pass through an MFC. This evaluation was necessary

164 because, in the main experimental setup, a portion of the excess flow must pass through an MFC,

165 to ensure that the excess flow rate is maintained at the desired value of 4 L min^{-1}, before being

166 directed to a chemical composition measurement instrument.

167   In this test, the AAC was continuously supplied with polydisperse ammonium sulfate

168 particles at various concentrations. An ammonium sulfate solution of 5 g L^{-1} was atomized using

169 a constant output atomizer (TSI 3076). Part of the atomized ammonium sulfate passed through a

170 HEPA filter and part went directly to the AAC to control the measured concentrations (Fig. S3).

171 The monodisperse flow and the excess flow rates were controlled with separate MFCs at 1.5 L

172 min^{-1} and 4 L min^{-1}, respectively, having a combined flow equal to 5.5 L min^{-1}. The ammonium

173 sulfate aerosol passing though the MFCs was sampled by an SMPS (TSI 3034) sampling at 1 L

174 min^{-1} and the remaining 4.5 L min^{-1} was exhausted with the help of a pump. As in the previous

175 test, a bypass line connected the SMPS to the front of the AAC and the SMPS sampling alternated

176 between the bypass line and the outlet flows of the AAC every 30 min over a 2-hour period. The

177 concentrations sent to the system were stable, so the long time-interval did not affect the accuracy

178 of the results.

179   The AAC cut-off was again set to an aerodynamic diameter of 140 nm, corresponding to a

180 d_{50} electrical mobility diameter of 100 nm (Fig. S4). Mass penetration efficiency was calculated,

181 as before, by comparing the average mass size distributions measured by the SMPS between the

182 bypass line and the outlet flows line. At the 100 nm electrical mobility diameter cut-off, the mass

183   penetration was 50%, while for particles between 50-100 nm it was over 80% (Fig. S4). These

184   results confirm that the system exhibits minimal losses, even when aerosol flows pass through

185   MFCs for $PM_{0.1}$.

186

187   **2.2 The continuous $PM_{0.1}$ chemical characterization system**

188   A schematic of the experimental set-up is shown in Fig. 2. The ambient inlet air first passed through

189   a $PM_{2.5}$ Sharp Cut Cyclone (SCC; AAVOS International) at 16.7 L min^{-1}, to extend the interval

190   between required cleanings of the AAC's outer cylinder, where larger particles impact.

191
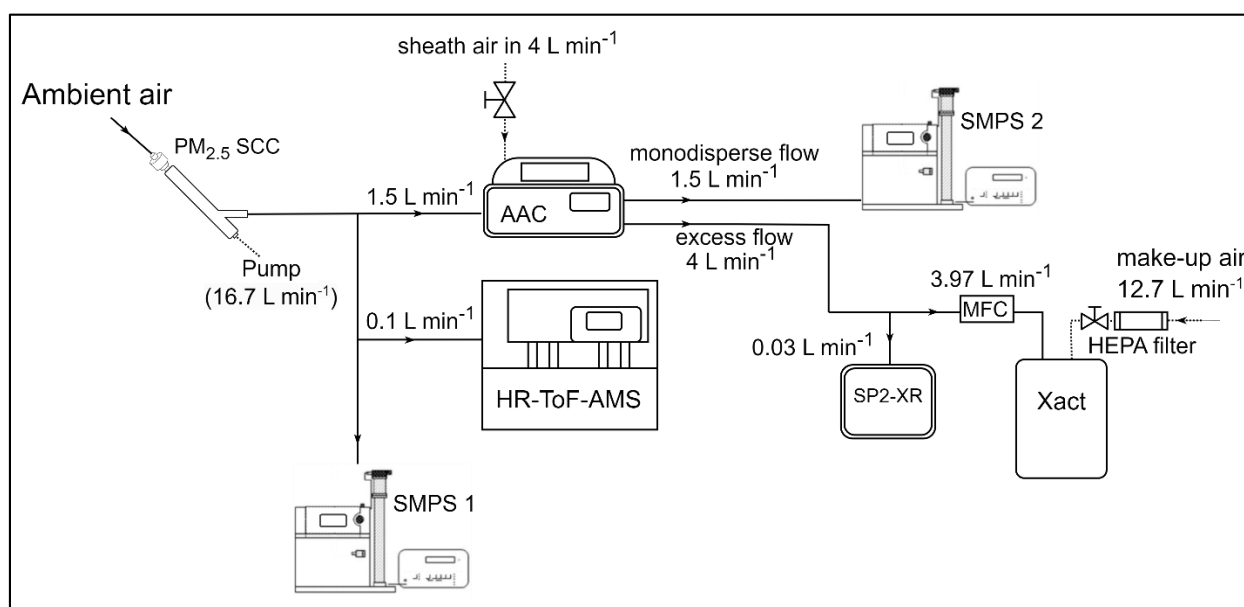
193   **Figure 2. Experimental set-up for the continuous $PM_{0.1}$ chemical characterization system.**

194

195   The ambient aerosol size distribution was measured by an SMPS (SMPS-1; TSI Classifier

196   model 3080, DMA model 3081, CPC 3775), and its size/ composition distribution by a High-

197   Resolution Time-of-Flight Aerosol Mass Spectrometer (HR-ToF-AMS; Aerodyne Research Inc.;

198   DeCarlo et al., 2006). The SMPS-1 continuously measured the total $PM_{0.1}$ and provided size

199   distributions for electrical mobility diameters from 10 nm to 505 nm, with a sample flow of 1 L

200   min^{-1} and a sheath flow of 5 L min^{-1}. The HR-ToF-AMS measured the size-resolved chemical

201   composition of sub-micrometer aerosols (specifically organics, nitrate, sulfate, chloride, and

202   ammonium). The vaporizer surface temperature was 600°C. The HR–ToF–AMS data was gathered

203   at three-minute intervals with sampling flow at approximately 0.1 L min^{-1}.

204   The AAC was operating as a $PM_{0.1}$ separator, with the d_{50} cut diameter set at 140 nm
205 aerodynamic diameter (100 nm electrical mobility diameter, and physical diameter for spherical
206 particles). The AAC was set to operate with a polydisperse inlet flow equal to 1.5 L min^{-1}, and
207 provided two outlet flows: (1) the monodisperse outlet flow, which was controlled at 1.5 L min^{-1},
208 and directly sent to a second SMPS (SMPS 2; TSI Classifier model 3080, DMA model 3081, CPC
209 3787), and (2) the excess outlet flow, which contained the smaller than the selected cut-off particles
210 and was controlled at 4 L min^{-1}. This excess outlet flow was analyzed using two instruments. A
211 single-particle soot photometer (SP2-XR; Droplet Measurement Technologies), measured
212 refractory black carbon (rBC) continuously, and had a sample flow of 0.03 L min^{-1} and a sheath
213 flow of 0.06 L min^{-1}. An Xact 625i (SailBri Cooper Inc.), measured concentration of elements
214 semi-continuously (4-hour sampling).

215   The Xact samples with a 16.7 L min^{-1} flow. To ensure that the excess outlet flow from the
216 AAC remained at 4 L min^{-1}, the aerosol sampled by the Xact passed through an MFC set at 3.97 L
217 min^{-1}. This value was calculated by subtracting the SP2-XR sampling rate of 0.03 L min^{-1} from the
218 desired total of 4 L min^{-1}. The remaining 12.73 L min^{-1} of the Xact sample flow was provided as
219 clean air, which diluted the samples measured by the Xact by approximately 11.

220   Ambient $PM_{0.1}$ chemical composition measurements were performed in Patras (38° 17' N
221 21° 48' E), Greece, at the Institute of Chemical Engineering Sciences (ICE-HT/ FORTH) between
222 17-29 July 2024. The station is located in a suburban area approximately 9 km northeast of the city
223 center. During summer in southern Greece, ambient temperatures are typically high, and relative
224 humidity is below 40% (Fig. S5), so the inlet air was not dried for these measurements. All
225 sampling lines used in this study were stainless steel to avoid potential artifacts from conductive
226 silicone tubing (Timko et al., 2009).

227   For a three-day period (July 29 to 1 August) the HR-ToF-AMS was set up to collect spectra
228 attributed specifically to $PM_{0.1}$ by positioning it downstream of the AAC, configured to function
229 as a $PM_{0.1}$ separator, again with a d_{50} set at 140 nm aerodynamic diameter, and with the same flow
230 settings as in the previous experimental set-up (Fig. 3). The monodisperse outlet flow was
231 controlled with an MFC at 1.5 L min^{-1} and in this case exhausted through a pump. The excess
232 outlet flow containing the particles smaller than the selected cut-off was sampled by the HR-ToF-
233 AMS and by an SMPS (TSI Classifier model 3080, DMA model 3081, CPC 3775). The SMPS had
234 a sample flow equal to 0.6 L min^{-1} and was used to calculate the AMS collection efficiency. The

235   remaining 3.3 L min^{-1}, out of the total 4 L min^{-1} that was the controlled flow rate of the excess

236   flow, was exhausted through a pump.

237

238
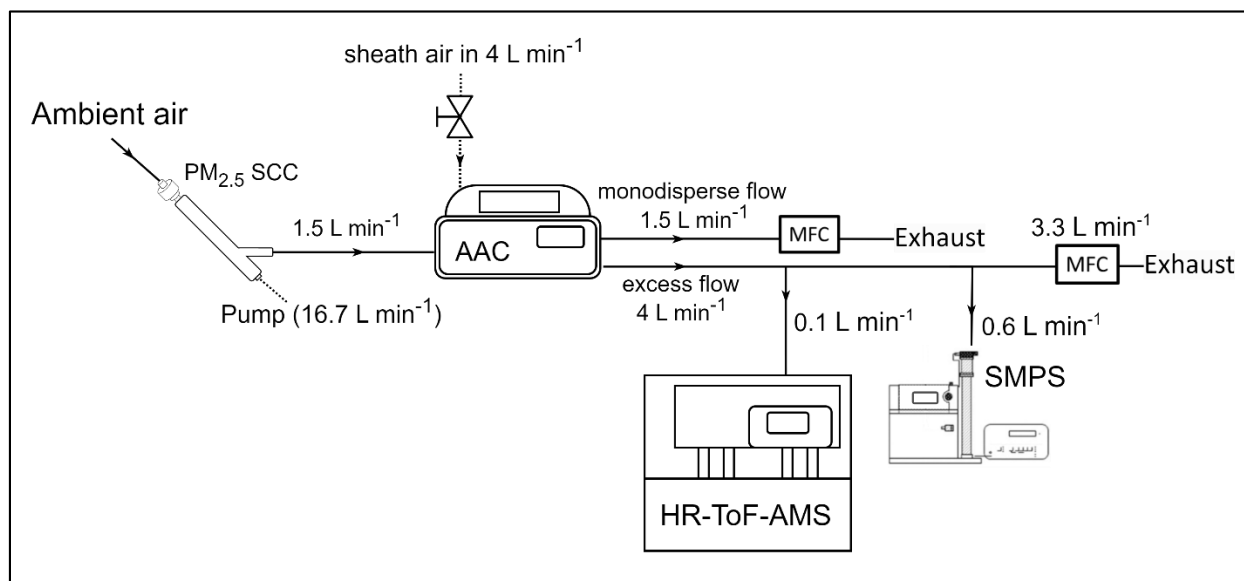
239   **Figure 3. Experimental set-up for the continuous source apportionment of PM$_{0.1}$ organic**

240   **aerosol (OA).**

241

242   **3. Data analysis**

243   **3.1 HR-ToF-AMS data analysis**

244   The AMS data was processed using the standard SQUIRREL software (v1.66E) within Igor Pro

245   (Wavemetrics), along with the PIKA package (v1.26E) for high-resolution peak integration.

246   Elemental ratios measured by the HR-ToF-AMS were determined using the improved ambient

247   calculation method proposed by Canagaratna et al. (2015). The collection efficiency (CE) for the

248   HR-ToF-AMS was assessed by combining HR-ToF-AMS mass distributions (vacuum

249   aerodynamic diameters approximately from 40 to 150 nm) with the SMPS-1 volume distributions

250   (electrical mobility diameters from 10 to 100 nm) and applying the Kostenidou et al. (2007)

251   algorithm every two hours. The same algorithm was used to determine the PM$_1$ organic aerosol

252   (OA) density. The upper limit of the HR-ToF-AMS mass distributions, approximately 150 nm

253   vacuum aerodynamic diameter, was selected based on the particle density of the measured aerosol.

254   For a particle density of 1.5 g cm^{-3} and spherical particles, this corresponds to a physical diameter

255   of about 100 nm (DeCarlo et al., 2004), consistent with the PM$_{0.1}$ definition used in this study.

256   AMS data between 17-29 July 2024 were then averaged over 4-hour intervals to align with the

257   Xact dataset, with negative values replaced with zero values.

258

259   **3.2 Xact625i data analysis**

260   The 4-hour Xact samples were corrected for both positive artifacts and dilution effects. The Xact

261   uses reel-to-reel Teflon filter tape sampling and nondestructive energy dispersive X-ray

262   fluorescence (EDXRF) analysis (Furger et al., 2017; Tremper et al., 2018). While this analytical

263   method is highly effective even for low concentrations, it is susceptible to positive artifacts,

264   especially in multi-element ambient samples, where spectral line interferences are common and

265   can hinder the detection of a specific element when another is present at high concentrations

266   (Furger et al., 2017). To address positive artifacts in the Xact samples and to determine the limit

267   of detection (LOD) for each element, blank measurements were conducted. For these blank

268   measurements, a HEPA filter was placed upstream of the $PM_{2.5}$ cyclone to assess potential artifacts

269   introduced by components situated between the ambient air inlet and the Xact (Fig. 2). These

270   components included the tubing, the $PM_{2.5}$ cyclone, the AAC, and one MFC, which are constructed

271   from different metallic materials and could potentially introduce contamination. The LOD for each

272   element *i* was calculated following the IUPAC Recommendations (Currie, 1995) and the JRC

273   Publications Repository (Majcen et al., 2012) using the equation:

274

276    $$\text{LOD}_i = \mu_{\text{blank},i} + k_\alpha \sigma_{0,i} + k_\beta \sigma_{0,i}, \tag{1}$$

275

277   where $\mu_{\text{blank},i}$ represents the mean value of the blank measurements for element *i*, and $\sigma_{0,i}$ is the

278   standard deviation of the blank measurements for the same element. The terms k_α and k_β are

279   numerical factors associated with the α-error and β-error, respectively. The α-error corresponds to

280   the risk of falsely detecting the analyte when it is not present, while the β-error corresponds to the

281   risk of failing to detect the analyte when it is present. These factors are chosen based on the desired

282   confidence level. For a 90% confidence level for both α-error and β-error, and 3 degrees of freedom

283   (calculated as the number of our blank samples minus 1), k_α and k_β are equal to one-tailed

284   Student's *t* value. In this case, $k_\alpha = k_\beta = 1.64$. Substituting these values into Eq. (1) simplifies

285   to:

286

287     $\text{LOD}_i = \mu_{\text{blank},i} + 3.3\,\sigma_{0,i},$ (2)

288

289   The field blank values and calculated LOD values for the detected elements are summarized in

290   Table S1 to illustrate the background levels observed for each detected element. It should be noted

291   that LOD values can vary considerably depending on factors such as the sampling lines, the

292   cleanliness of the Xact tape, and other operational parameters, as well as the degrees of freedom

293   and confidence levels applied in the LOD calculation formulas. Therefore, blank measurements

294   and LOD calculations should be performed for every field deployment to ensure proper assessment

295   of the Xact's performance and to enable accurate data interpretation, regardless of the results

296   presented here.

297   The dilution factor for the Xact samples (DF_{Xact}) was calculated based on the total air

298   volume that was measured by the Xact for each sample (V_{Xact}), which can be slightly different

299   from sample to sample, depending on ambient temperature. So, the DF_{Xact} combining also the

300   dilution factor by the AAC (DF_{AAC}) working as a $\text{PM}_{0.1}$ separator was calculated as:

301

303     $\text{DF}_{\text{Xact}} = \dfrac{V_{\text{Xact}}}{3.97\,t}\,\text{DF}_{\text{AAC}},$ (3)

302

304   where t is the sampling time in minutes, and 3.97 L min^{-1} represents the flow rate into the Xact

305   after the AAC-$\text{PM}_{0.1}$-separator (Fig. 2). The sampling time for the 4-hour samples was 240 min.

306   The Xact performs an automated quality assurance test every midnight, which reduces the

307   sampling time of the midnight samples by approximately 30 min. The DF_{Xact} values varied from

308   9.7 (for the midnight samples) to 11.15. Each Xact sample was corrected based on its specific

309   DF_{Xact}.

310   The Xact detected the elements Si, S, Cl, K, Ca, Ti, Fe and Zn (Fig. S6). During the summer

311   months in Patras, $\text{PM}_{0.1}$ concentrations are typically low (Argyropoulou et al., 2024), resulting in

312   measured element concentrations that were close to their respective limits of detection (LODs). In

313   X-ray spectrometry, as with most analytical techniques, matrix effects in ambient samples, caused

314   by interactions between different elements and varying analyte concentrations, can lead to higher

315   and more variable LODs across samples. Measurement uncertainties are particularly pronounced

316   near the LOD for elements susceptible to spectral interferences in multi-element samples, as well

as for lighter elements (Si, S, Cl, K, and Ca), which tend to be more affected by self-absorption effects (Furger et al., 2017). Although this uncertainty is generally independent of the Xact's tube temperature, Si exhibited a moderate to high correlation ($R^2 = 64\%$) with the tube temperature of the instrument (Fig. S7). Due to this potential temperature-related artifact, Si was excluded from the main results. The levels of the rest of the detected elements had low to no correlation with the tube temperature of the instrument.

The Xact 4-hour samples that were below their respective LODs were replaced with zero values. The elements S, Cl, K, Ca, Ti, Fe and Zn were corrected by subtracting their respective blank value and then multiplying the non-negative values by the respective sample-dilution-factor (Eq. (3)) (Fig. S8). The uncorrected and the corrected values of the elements detected by the Xact in this study are summarized in Table S2.

The corrected average values of S and Cl from the Xact were compared with the average sulfate and chloride concentrations measured by the AMS. During the measurement period from 17 to 29 July 2024, the average S concentration from the Xact (multiplied by 3 to match the sulfate concentrations by the AMS) was on average 96.2 ng m^{-3}, closely aligning with the AMS-measured sulfate concentration of 100.7 ng m^{-3}. The average Cl concentration from the Xact was 7.2 ng m^{-3}, compared to 13.5 ng m^{-3} for chloride from the AMS. Although this agreement is not as strong as that for S/sulfate, it is reasonable, especially considering that chloride accounted for less than 2% of total PM$_{0.1}$, making precise quantification inherently challenging. In this context, the fact that the two measurements were of the same order of magnitude and differed by only a few nanograms was a satisfactory outcome. The correlation between Xact and AMS measurements over shorter time intervals was low. This can be attributed to measured values being near their respective limits of detection (LODs) and uncertainties associated with the measurement of light elements. Moreover, the low number of measured samples means that even a few mismatched data points can significantly reduce the correlation between datasets. Thus, for the main results, the timeseries of sulfate and chloride concentrations measured by the AMS are shown, rather than the S and Cl measurements from the Xact. For the remaining measured elements and the complete PM$_{0.1}$ composition, only average values over the entire measurement period (17–29 July 2024) are shown, as Xact measurements for shorter time intervals were deemed rather uncertain for these low PM$_{0.1}$ concentrations of the sampling location.

4. Ambient $PM_{0.1}$ chemical composition

The $PM_{0.1}$ estimated from the SMPS-1 measurements for an effective density equal to 1.5 g cm^{-3}, had an average concentration of 0.69 ± 0.28 μg m^{-3}, ranging from minimum 0.4 μg m^{-3} to maximum 1.5 μg m^{-3} (15 min averages) (Fig. 4). $PM_{0.1}$ peaked in the morning, between 6:00 and 8:00 local time (LT), primarily due to increased rBC concentrations associated with morning traffic (Fig. 5). Concentrations of all $PM_{0.1}$ species increased during the evening from 20:00 LT to midnight.

The average refractory $PM_{0.1}$ BC concentration was 0.038 ± 0.074 μg m^{-3}, with values ranging from a minimum of 0.003 μg m^{-3} to a maximum 0.059 μg m^{-3} (15 min averages) (Fig. 4). $PM_{0.1}$ rBC peaked during early morning hours (07:00 LT) and had a smaller peak in the evening (20:00–24:00 LT) (Fig. 5). On average, rBC contributed 4% to total $PM_{0.1}$, with contributions ranging from 1% to 19% at hourly scales (Fig. 6).

The organic $PM_{0.1}$ mass concentration had an average value of 0.34 ± 0.17 μg m^{-3} (Fig. 4), making it the largest contributor to total $PM_{0.1}$ (45% on average ranging from 23% to 71%; 4-h averages). The $PM_{0.1}$ OA concentrations remained relatively stable, with minor peaks at night (22:00 LT) and early in the morning (06:00 LT) (Fig. 5).

Sulfate had an average concentration of 0.1 ± 0.05 μg m^{-3} (Fig. 4) and contributed 14% to $PM_{0.1}$ on average (Fig. 6), with contributions ranging from 6% to 25% (4-h averages). Sulfate concentrations peaked early in the morning (06:00 LT) and showed a secondary, less pronounced increase at night (22:00 LT) (Fig. 5).

Both OA and sulfate exhibit relatively stable diurnal profiles, with slight increases in the morning and evening, and a slight decrease around midday. These morning and evening increases are accompanied by rises in BC, indicating local traffic as a likely source. An additional and plausible explanation involves boundary layer dynamics. During midday, the boundary layer height typically increases, leading to enhanced vertical mixing and dilution of pollutants, which in turn reduces their near-surface concentrations. In suburban environments, this dilution can outweigh midday photochemical production unless there is a significant influx of secondary organic aerosol (SOA) precursors.

Ammonium had an average concentration of 0.06 ± 0.07 μg m^{-3}, while nitrate averaged 0.02 ± 0.01 μg m^{-3} (Fig. 4). Their contributions to $PM_{0.1}$ were 7% (ranging from 1% to 19%) and 3% (ranging from 1% to 6%), respectively for the 4-hour averages (Fig. 6). Both ammonium and

378
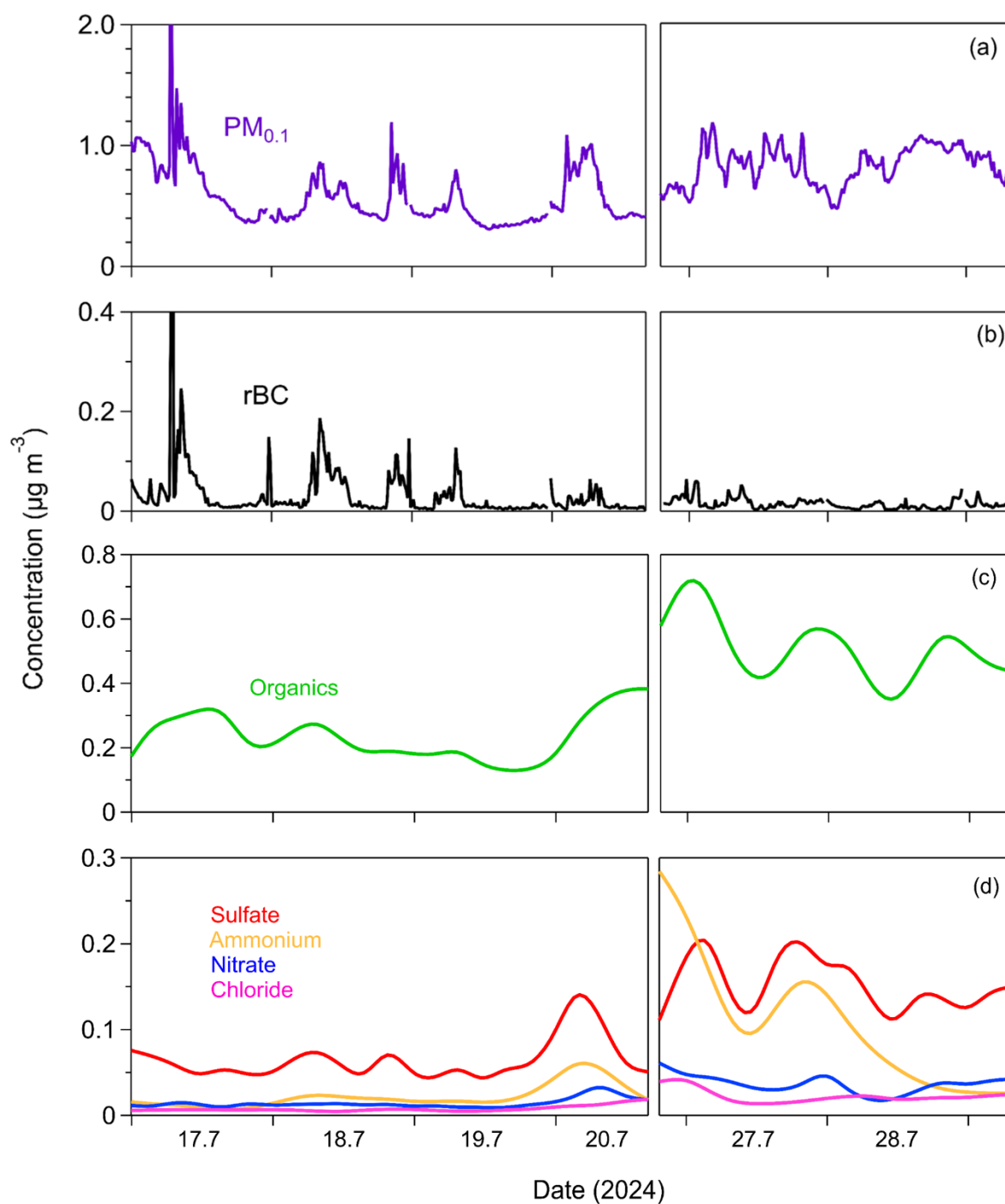
Figure 4. Timeseries of (a) particle mass concentration of particles with diameters below 0.1 μm (PM$_{0.1}$) measured by SMPS-1, (b) PM$_{0.1}$ refractory black carbon (rBC) measured by the SP2-XR (c) PM$_{0.1}$ organics (d) PM$_{0.1}$ sulfate, ammonium, nitrate and chloride measured by the HR-ToF-AMS, in Patras, Greece, from 17 to 29 July 2024. The time resolution for PM$_{0.1}$ and rBC is 15 min, while for organics, sulfate, ammonium, and nitrate the time resolution is 4 hours.

385 nitrate concentrations peaked at night (22:00 LT) and decreased to their minimum levels midday

386 (14:00 LT) (Fig. 5).

387   Chloride had an average concentration of 0.013 ± 0.010 µg m^{-3} (Fig. 4). Its concentration

388 was relatively stable, with a slight increase late at night (02:00 LT) (Fig. 5). Chloride contributed

389 an average of 1.7% to PM$_{0.1}$, with contributions ranging from 0.4% to 4% for the 4-hour averages

390 (Fig.6).

391   The hourly averages of organic, sulfate, ammonium, nitrate, and chloride are shown

392 alongside the hourly rBC data in Fig. S9. In most cases, the morning rBC peaks coincide with

393 increases in organic PM$_{0.1}$. While higher time resolution can be particularly useful for a more

394 detailed examination, the 4-h averaging still effectively illustrates the temporal trends of each

395 species.

396   The corrected mean concentrations of elements in PM$_{0.1}$ measured by the Xact followed

397 the order: Ca > Fe > K > Zn > Ti (Fig. S8). The average mass concentrations were 130 ng m^{-3} for

398 Ca, 29.6 ng m^{-3} for Fe, 19.6 ng m^{-3} for K, 1.4 ng m^{-3} for Zn, and 1.1 ng m^{-3} for Ti. Their respective

399 contributions to PM$_{0.1}$ were 18.2% for Ca, 4.3% for Fe, 2.8% for K, 0.2% for Zn, and 0.2% for Ti

400 (Fig. 6). Refractory components such as Ca, Fe, K, Zn, and Ti typically exist in the form of oxides,

401 although their exact chemical form often remains uncertain (Seinfeld and Pandis, 2016). For this

402 reason, we report only their elemental concentrations, as this is the direct output of the Xact

403 measurements.

404   The daily averages of the summed concentrations of all measured species (organics, sulfate,

405 ammonium, nitrate, chloride, rBC, Ca, Fe, K, Zn and Ti) were compared to the daily average PM$_{0.1}$

406 concentrations estimated from SMPS-1 measurements, for effective density of 1.5 g cm^{-3} (Fig. 6).

407 This comparison was performed to assess their agreement and evaluate the closure of the chemical

408 balance of PM$_{0.1}$. The best-fit regression line had a slope of 0.75 and an intercept of 0.21 µg m^{-3},

409 with an R^2 value of 42%. When constrained to pass through zero, the regression line had a slope

410 of 1.03. Most of the daily averages fell within the ±20% deviation lines, with the remainder within

411 ±40%.

412

413 **5. Effective density estimation of PM$_{0.1}$**

414 The effective density (ρ_{eff}) of PM$_{0.1}$ was estimated in this study using two approaches. The first

415 approach was by estimating ρ_{eff} from the measured chemical composition of PM$_{0.1}$. For this

416
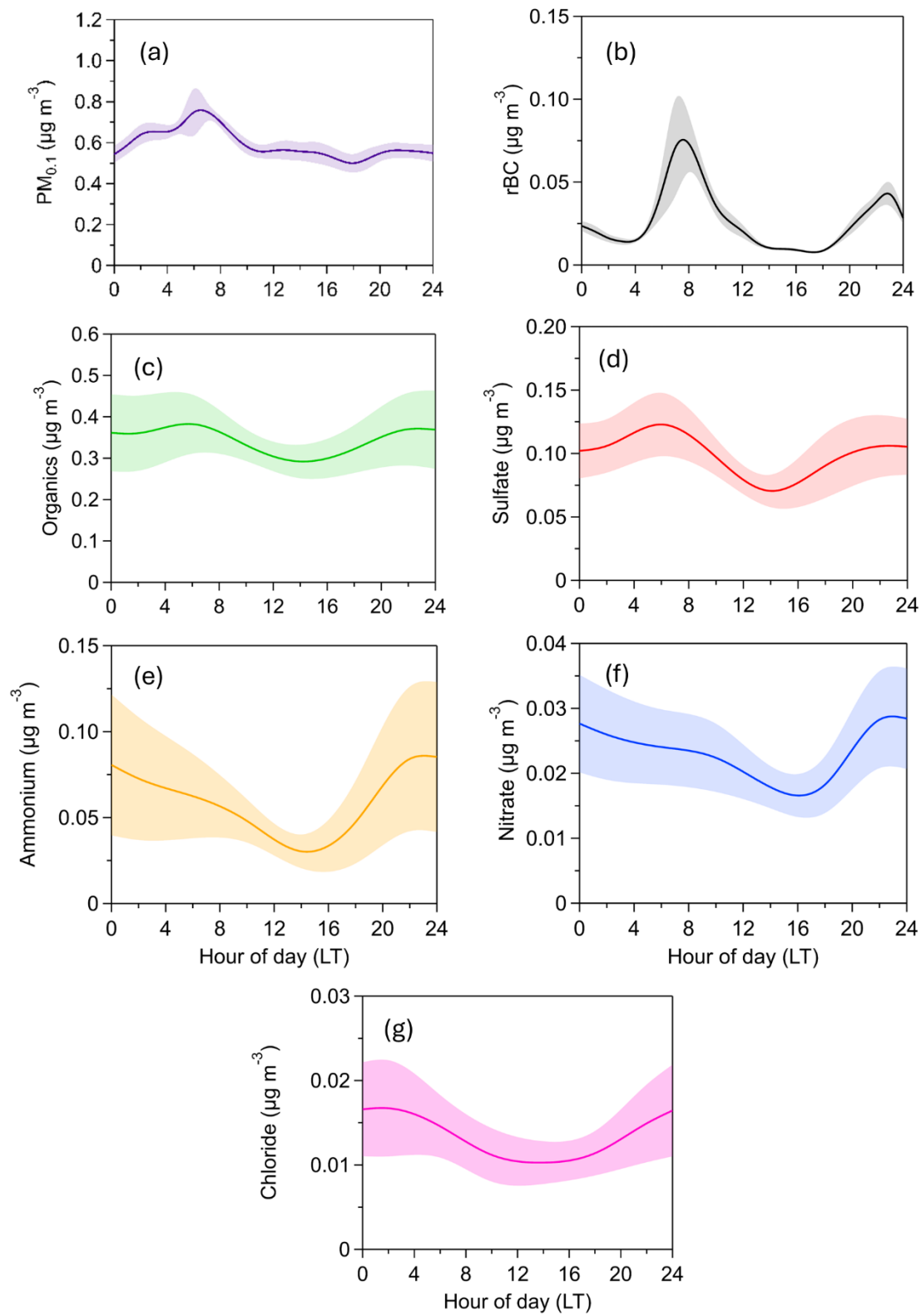
Figure 5. Diurnal variation of PM$_{0.1}$ concentration and composition. The shaded areas correspond to the standard deviation of the mean.

approach, the OA hourly effective density was calculated by the Kostenidou et al. (2007) algorithm. A density of 1.8 g cm^{-3} was assumed for BC (Taylor et al., 2015). The effective density of PM$_{0.1}$ derived from the chemical composition measurements was 1.47 ± 0.02 g cm^{-3} (Fig. 7).

The second approach for the PM$_{0.1}$ ρ_{eff} estimation was by continuously directing the monodisperse ambient aerosol from the AAC (set at 140 nm aerodynamic diameter) to the SMPS-2 (AAC/SMPS in tandem; Tavakoli and Olfert, 2014) (Fig. 2). This setup produced a monodisperse aerosol distribution with an electrical mobility diameter of approximately 100 nm (Fig. S10). For spherical particles, this electrical mobility diameter is equivalent to the physical diameter (Hinds, 1999; DeCarlo et al., 2004). This estimation method relies solely on the monodisperse distribution of 100 nm particles and provides a rapid and straightforward means to approximate ρ_{eff} for PM$_{0.1}$. Given that the majority of PM$_{0.1}$ lies near 100 nm, deriving the effective density in this range offers a reasonable estimate of the ρ_{eff} for PM$_{0.1}$.
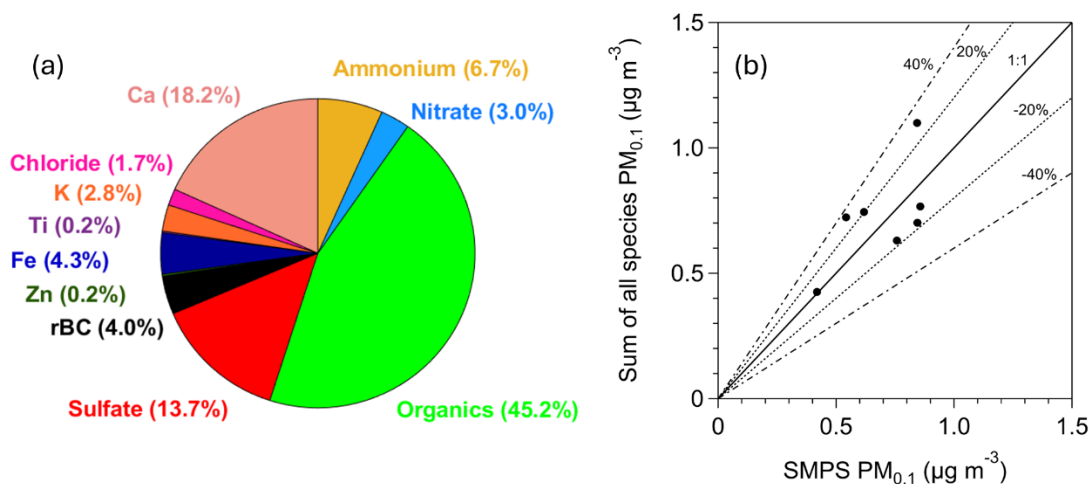
Figure 6. (a) Average PM$_{0.1}$ chemical composition for the period of measurements (17 to 29 July 2024) in Patras, Greece. (b) Daily average of the sum of the measured PM$_{0.1}$ species versus daily average of the PM$_{0.1}$ measured by the SMPS, for effective density equal to 1.5 g cm^{-3}. The black line corresponds to the 1:1 line, and the dashed lines correspond to the ± 20% and ± 40%, respectively.

The particle's electrical mobility (B) is calculated using the electrical mobility diameter (d_{mo}) measured by the SMPS-2:

442 $$B = \frac{C_c(d_{\mathrm{mo}})}{3\pi\mu d_{\mathrm{mo}}}, \tag{4}$$

441

443 where μ represents the viscosity of the carrier gas, and C_c is the Cunningham slip correction factor

444 for the corresponding d_{mo} (Kim et al., 2005). The hourly average of the peak of the monodisperse

445 distribution measured by the SMPS-2 was used for d_{mo} (Fig. S10).

446   The particle's mass (m) is then calculated using the derived B and the aerodynamic diameter

447 (d_{ae} = 140 nm) set on the AAC:

448

450 $$m = \frac{C_c(d_{\mathrm{ae}})\rho_0 d_{\mathrm{ae}}^2}{18\mu\, B}, \tag{5}$$

449

451 where C_c is the Cunningham slip correction factor of the corresponding d_{ae} (Kim et al., 2005), and

452 ρ_0 is the reference density equal to 1000 kg m^{-3}. Finally, the ρ_{eff} can be expressed as:

453

455 $$\rho_{\mathrm{eff}} = \frac{m}{(\pi/6)\, d_{\mathrm{mo}}^3}, \tag{6}$$

454

456 Substituting m from Eq. (5) into Eq. (6) allows the calculation of ρ_{eff}.

457   The effective density derived from the AAC/SMPS in tandem approach was on average

458 1.51 ± 0.04 g cm^{-3}, consistent with the PM$_{0.1}$ ρ_{eff} that was determined through chemical

459 composition measurements (Fig. 7). The average effective density over the measurement period

460 derived from both approaches (estimation by chemical composition, and estimation by

461 AAC/SMPS in tandem) was equal to 1.5 g cm^{-3}. This value has been consistently applied

462 throughout this study.

463

464 **6. Sources of PM$_{0.1}$ organic aerosol**

465 To identify the various sources of OA, Positive Matrix Factorization (PMF) analysis was

466 conducted, using high-resolution AMS organic mass spectra (m/z values from 12 to 120) as input

467 data (Paatero and Tapper, 1994; Lanz et al., 2007; Ulbrich et al., 2009) for a three-day period (July

468   29 to 1 August). The PMF analysis, applied to a high-temporal-resolution dataset of approximately

469   700 data points (3-minute intervals), yields reasonable results.

470   Analysis was performed using both the unconstrained PMF method (Ulbrich et al., 2009)

471   and the Multilinear Engine algorithm (ME-2; Paatero, 1999), with the latter at varied α values

472   using the Source Finder (SoFi) software (Canonaco et al., 2013). The factors in both methods

473   varied from one to seven, and different f_{peak} values were tested, ranging from −1 to 1 in 0.2

474   increments. ME-2 is helpful when PMF results are inconclusive or when smaller source

475   contributions need better quantification. In this study, results obtained using the unconstrained

476   PMF approach using SoFi are referred to simply as "PMF," while those derived from the

477   constrained ME-2 implementation using SoFi are referred to as "ME-2". The primary difference

478   between the two methods is that ME-2 allows users to input prior information on factor profiles,

479   forcing the algorithm to account for specific sources.

480

481
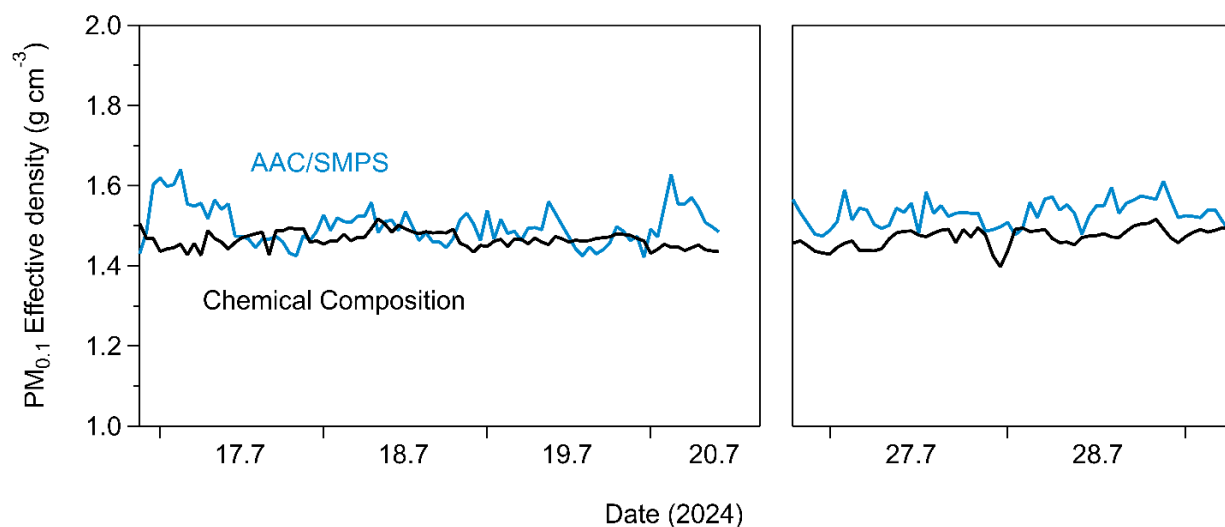
482   **Figure 7. Hourly effective density of PM$_{0.1}$ estimated by the chemical composition**

483   **measurements (black line) and by combining the AAC with an SMPS (blue line) (Tavakoli**

484   **and Olfert, 2014).**

485

486   A two-factor solution in PMF was initially explored to assess the composition of PM$_{0.1}$ OA.

487   This analysis identified two distinct secondary organic aerosols (SOA) factors: a more-oxidized

488   oxygenated organic aerosol (MO-OOA) factor and a less-oxidized oxygenated organic aerosol

489   (LO-OOA) factor. The MO-OOA accounted for 58% of the PM$_{0.1}$ OA mass, with an O:C ratio of

490   0.8, indicating a higher degree of oxidation. In contrast, the LO-OOA contributed 42% of the PM$_{0.1}$

491   OA mass and exhibited a lower O:C ratio of 0.6. Notably, the high-resolution (HR) spectra of the

492   two factors were highly similar (R^2=0.96), and their time series showed strong anticorrelation (Fig.

493   S11). These findings suggested that a two-factor solution might oversimplify the data and that a

494   more nuanced representation could be achieved by increasing the number of factors.

495   To better characterize the sources of PM$_{0.1}$ OA, a three-factor solution was subsequently

496   adopted in the PMF analysis. This approach resolved three oxygenated organic aerosol (OOA)

497   factors: a more-oxidized OOA (MO-OOA) factor, a less-oxidized OOA (LO-OOA) factor, and an

498   oxidized primary OA (OPOA) factor (Fig. 8). The average O:C ratio during this period was 0.64

499   ± 0.04, implying that indeed the PM$_{0.1}$ aerosol was rather aged. The HR spectra for the three

500   resolved OA factors are presented in Fig. S12.

501
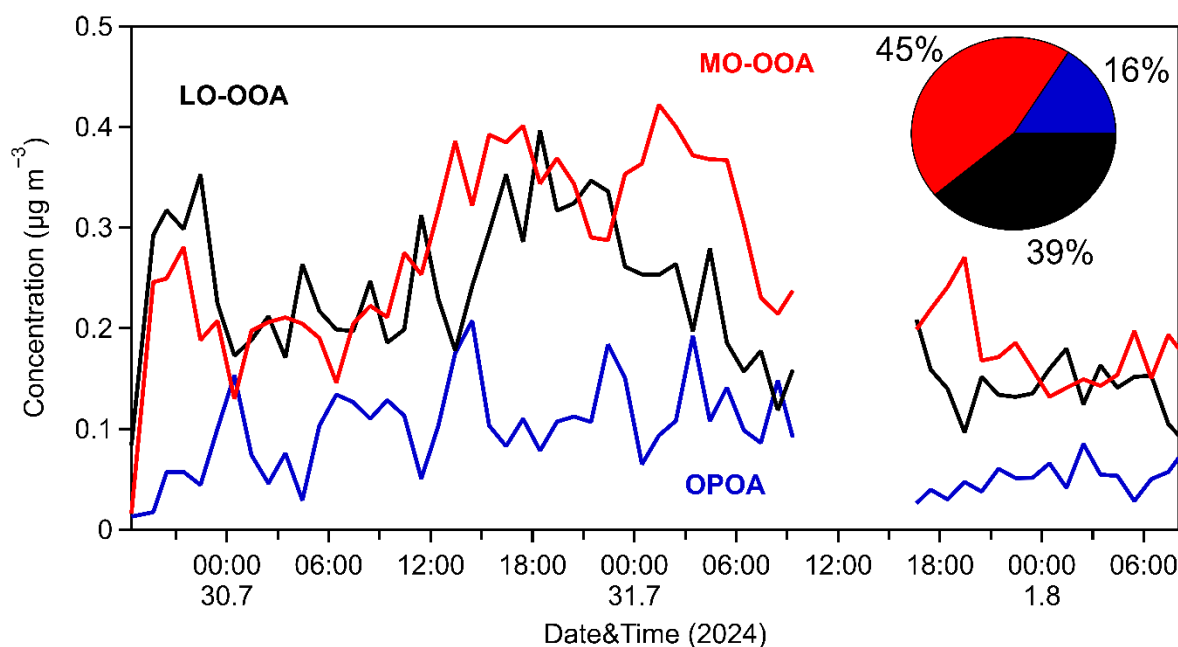
503   **Figure 8. Hourly time-series of the PMF factors for PM$_{0.1}$ OA**.

504

505   The MO-OOA factor dominated during the 3-day measurement period, representing

506   around 45% of the PM$_{0.1}$ OA with an average concentration of 0.25 μg m^{-3}, while its hourly

507   maximum value was equal to 0.4 μg m^{-3}. Its O:C was 0.96 and its correlation to PM$_{0.1}$ sulfate and

508   nitrate was medium (R^2 = 0.43 and 0.48, respectively). The LO-OOA contributed 39% to OA with

509   a mean value of 0.2 µg m^{-3}. Its O:C was equal to 0.6 and correlated reasonably well with particulate

510   PM$_{0.1}$ sulfate (R^2 =0.60) (Fig. S13). Both MO-OOA and LO-OOA factors were dominated by

511     $C_xH_yO^+$ and $C_xH_yO_z^+$ families (62% and 50%, respectively), while the $C_xH_y^+$ family was

512   responsible for 21% (MO-OOA) and 36% (LO-OOA) of each spectrum. An OPOA factor was

513   identified as the third factor during the measurements, characterized by intermediate O:C of 0.42,

514   indicative of moderate chemical aging occurring during or shortly after emission. It represented

515   16% of the PM$_{0.1}$ OA. Its mass spectrum exhibited features that distinguish it from both POA and

516   secondary organic aerosols (SOA) and features prominent peaks at m/z 28 (CO^+), 43 ($C_2H_3O^+$),

517   and 44 (CO_2^+), reflecting the presence of oxygen-containing functional groups. While its spectrum

518   retains characteristic peaks of primary organic aerosols (POA) such as hydrocarbon-like OA

519   (HOA) and cooking OA (COA), its relatively higher oxygen content suggests that emitted OA had

520   undergone partial atmospheric oxidation. The OPOA spectrum was dominated by the $C_xH_y^+$ family

521   (45%), while the $C_xH_yO^+$ and $C_xH_yO_z^+$ families together account for approximately 40% of the

522   spectrum (Fig. S12). Key peaks appear at m/z 27, 28, 29, 41, 43, 44, 53, 55, 67, 69, 81, 83 and 91.

523   Its average concentration was 0.09 µg m^{-3} and its O:C was consistent with similar OPOA factors

524   reported in Beijing by Xu et al. (2019). OPOA showed a moderate correlation with particulate

525   PM$_{0.1}$ NO$_3$ ($R^2 = 0.41$) (Fig. S14).

526   The absence of fresher factors in the PMF solution suggested the use of an external POA

527   spectrum. For this study, a HOA factor derived from a wintertime field campaign previously

528   conducted in Patras (Florou et al., 2017) was selected, ensuring compatibility with the study's

529   conditions. The α-value approach was employed, testing a range of α-values from 0 to 0.3 in

530   increments of 0.05 to assess the sensitivity of the results to rotational constraints.

531   A three-factor solution was selected in the ME-2 analysis as it provided the most effective

532   representation of the OA sources. This solution identified two SOA factors (MO-OOA and LO-

533   OOA) along with the constrained HOA factor (Fig. 9). The mass spectra for these factors are

534   presented in Fig. S15.

535   Over the three-day observation period, the LO-OOA factor contributed approximately 70%

536   of the total OA, with an average concentration of 0.4 µg m^{-3} and an O:C of 0.77. LO-OOA

537   correlated quite well with particulate PM$_{0.1}$ sulfate (R^2 =0.64) and nitrate (R^2 =0.50). Its spectrum

538   was dominated by oxygenated chemical families, which accounted for nearly 55% of the identified

539   fragments. The MO-OOA factor, representing the most chemically aged component, accounted for

540   19% of the total OA with a mean concentration of 0.1 μg m^{-3}. It exhibited an O:C ratio of 0.84,

541   with prominent spectral peaks at *m/z* 28 and 44, characteristic of highly oxidized organic

542   compounds. Its correlation to PM$_{0.1}$ sulfate and nitrate was low to medium (R^2 = 0.26 and 0.47,

543   respectively). The HOA factor was responsible for 11% of the measured OA with a mean

544   concentration of 0.06 μg m^{-3}. There was no correlation with PM$_{0.1}$ sulfate (R^2 less than 0.1), while

545   weak correlations were observed with nitrate (R^2=0.26) and chloride (R^2=0.23). HOA had an O:C

546   of 0.23, which is slightly higher than the typical values reported for freshly emitted HOA factors

547   from HR-ToF-AMS spectra in urban environments (≤0.1). This elevated oxygenation level is likely

548   attributable to the suburban location of the site, which is situated away from direct urban emissions

549   and thus subject to less fresh (and less oxidized) aerosol inputs. Notably, previous studies have

550   documented ambient HOA O:C within a similar range of 0.19–0.24 in suburban areas (Gilardoni

551   et al., 2014; Kostenidou et al., 2015; Wu et al., 2022). The HOA spectrum was characterized by a

552   high (57%) contribution of the $C_xH_y^+$ family (Fig. S15), and had prominent peaks at *m/z* 27, 29,

553   41, 43, 53, 55, 57, 67, 69, 71, 77, 79, 81, 83, and 91, all in accordance with previous studies

554   regarding HOA.

555

556
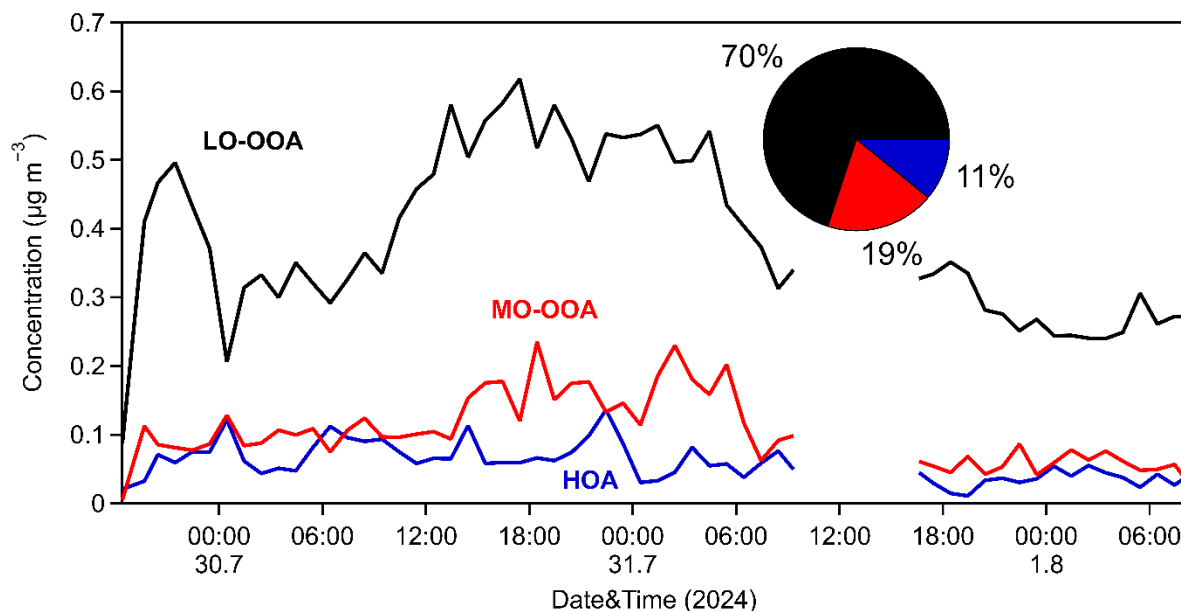
Figure 9. Hourly time-series of the ME-2 factors for PM$_{0.1}$ OA.

558

559   Upon comparing the solutions from the unconstrained PMF and ME-2 analyses, we

560   observe that the OPOA and HOA factors exhibit similar time-series behavior (Fig. S16), with peaks

561   occurring simultaneously. However, the OPOA factor shows more pronounced and higher peaks.

562   Both factors contribute similarly to $PM_{0.1}$ OA, accounting for 16% and 11%, respectively. The

563   primary difference between the ME-2 and PMF solutions lies in the contributions and spectra of

564   the MO-OOA and LO-OOA factors. In the ME-2 analysis, the MO-OOA factor contributes

565   significantly less (19% compared to 45% in the PMF analysis), while the LO-OOA factor

566   contributes substantially more (70% versus 39% in the PMF analysis) and displays a higher O:C

567   ratio than the LO-OOA factor in the PMF solution.

568   Figure S17 illustrates the ratio of *m/z* 43 to the total OA (f_{43}) against the ratio of *m/z* 44 to

569   the total OA (f_{44}) over the measurement period. These measurements are compared with the factor

570   solutions derived from both the PMF and ME-2 analyses. This analysis indicated that fresh HOA

571   had a surprisingly low contribution to $PM_{0.1}$ OA, if any. This is an interesting result that should be

572   investigated in future studies.

573

574   7. Conclusions

575   This study introduces a new method for the continuous chemical characterization of $PM_{0.1}$, using

576   an HR-ToF-AMS and an AAC operating as a $PM_{0.1}$-separator, followed by instruments that

577   measure BC and elements. The development and evaluation of this system was conducted in a

578   suburban area in Greece. These initial suburban measurements offer novel insights into the

579   chemical characteristics, effective density and organic aerosol sources of ultrafine PM.

580   OA was the most abundant component of $PM_{0.1}$. Sulfates and calcium were the next most

581   significant contributors, accounting for 14% and 18% of the total ultrafine mass, respectively.

582   Ammonium contributed 7%, refractory black carbon (rBC) accounted for 4% and the sum of

583   detected elements (Fe, K, Zn, Ti) for 7% of the total $PM_{0.1}$. Nitrate and chloride contributed less

584   than 4% each, at 3% and 2%, respectively. Source apportionment suggested the presence of three

585   sources of $PM_{0.1}$ OA. The majority of organic $PM_{0.1}$ was oxygenated OA, with contributions from

586   both more oxidized and less oxidized fractions, together comprising 80–90% of $PM_{0.1}$ OA. Primary

587   OA accounted for the remaining 10–15%.

588   The main limitation of the system at this point is the high dilution factor of the Xact. This

589   can be partially addressed through blank measurements and element-specific limits of detection

(LOD), but one potentially significant improvement would be to reduce the Xact's inlet sampling flow, which is factory-set at 16.7 L min^{-1}. While this flow rate is appropriate for ambient sampling of PM_1, $PM_{2.5}$ or PM_{10}, which was the instrument's original purpose, it proved to be not ideal for the $PM_{0.1}$ measurements investigated in this study. Enabling the Xact to operate effectively at lower sampling flows would significantly enhance its performance for $PM_{0.1}$ analysis.

Nonetheless, the proposed approach has the potential to serve as a robust research system for detailed chemical characterization of $PM_{0.1}$, especially in urban locations where there are typically higher $PM_{0.1}$ concentrations, and many more nearby sources. The system exhibited strong and reliable performance overall, and its deployment over longer monitoring periods to enable elemental source apportionment, alongside $PM_{0.1}$ OA and BC source apportionment, and in environments with more complex source profiles, than the one investigated in this pilot campaign, is a feasible and promising application for future campaigns. This detailed $PM_{0.1}$ chemical characterization approach can contribute towards deeper investigations and better understanding of the potential link between ultrafine particle mass and human health, or other issues of interest concerning ultrafine particles.

Data availability. The data from this work are available upon request from Spyros Pandis (spyros@chemeng.upatras.gr).

Supplement. The supplement related to this article is available online.

Author contribution. G.A. developed the chemical characterization system and performed the field measurements. G.A. and K.F. performed the corresponding data analysis and wrote the paper. S.N.P. directed the study and edited the paper.

Competing interests. The authors report there are no competing interests to declare.

Financial support. This work was funded by the project NANOSOMs Grant 11504 of the Greek HFRI.

ORCID. Georgia Argyropoulou https://orcid.org/0009-0009-9993-931X, Kalliopi Florou https://orcid.org/0000-0001-9766-656X, Spyros Pandis https://orcid.org/0000-0001-8085-9795.

References

Abdillah, S. F. I. and Wang, Y.-F.: Ambient ultrafine particle ($PM_{0.1}$): Sources, characteristics, measurements and exposure implications on human health, Environ. Res., 218, 115061, https://doi.org/10.1016/j.envres.2022.115061, 2023.

Argyropoulou, G. A., Kaltsonoudis, C., Patoulias, D., and Pandis, S. N.: Novel method for the continuous mass concentration measurement of ultrafine particles ($PM_{0.1}$) with a water-based condensation particle counter (CPC), Aerosol Sci. Technol., 58, 1182–1193, https://doi.org/10.1080/02786826.2024.2368196, 2024.

Baldauf, R., Devlin, R., Gehr, P., Giannelli, R., Hassett-Sipple, B., Jung, H., Martini, G., McDonald, J., Sacks, J., and Walker, K.: Ultrafine Particle Metrics and Research Considerations: Review of the 2015 UFP Workshop, Int. J. Environ. Res. Public. Health, 13, 1054, https://doi.org/10.3390/ijerph13111054, 2016.

Beauchemin, S., Levesque, C., Wiseman, C. L. S., and Rasmussen, P. E.: Quantification and Characterization of Metals in Ultrafine Road Dust Particles, Atmosphere, 12, 1564, https://doi.org/10.3390/atmos12121564, 2021.

Canagaratna, M. R., Jimenez, J. L., Kroll, J. H., Chen, Q., Kessler, S. H., Massoli, P., Hildebrandt Ruiz, L., Fortner, E., Williams, L. R., Wilson, K. R., Surratt, J. D., Donahue, N. M., Jayne, J. T., and Worsnop, D. R.: Elemental ratio measurements of organic compounds using aerosol mass spectrometry: characterization, improved calibration, and implications, Atmospheric Chem. Phys., 15, 253–272, https://doi.org/10.5194/acp-15-253-2015, 2015.

Canonaco, F., Crippa, M., Slowik, J. G., Baltensperger, U., and Prévôt, A. S. H.: SoFi, an IGOR-based interface for the efficient use of the generalized multilinear engine (ME-2) for the source apportionment: ME-2 application to aerosol mass spectrometer data, Atmospheric Meas. Tech., 6, 3649–3661, https://doi.org/10.5194/amt-6-3649-2013, 2013.

Cassee, Flemming, Morawska, Lidia, Peters, Annette, Wierzbicka, Aneta, Buonanno, Giorgio, Cyrys, Josef, SchnelleKreis, Jüergen, Kowalski, Michal, Riediker, Michael, Birmili, Wolfram, Querol, Xavier, Yildirim, Ali Önder, Elder, Alison, Yu, Il Je, Øvrevik, Johan, Hougaard, Karin Sørig, Loft, Steffen, Schmid, Otmar, Schwarze, Per E, Stöger, Tobias, Schneider, Alexandra, Okokon, Enembe, Samoli, Evangelia, Stafoggia, Massimo, Pickford, Regina, Zhang, Siqi, Breitner, Susanne, Schikowski, Tamara, Lanki, Timo, and Aurelio, Tobias: White Paper: Ambient ultrafine particles: evidence for policy makers., 2019.

Corsini, E., Vecchi, R., Marabini, L., Fermo, P., Becagli, S., Bernardoni, V., Caruso, D., Corbella, L., Dell'Acqua, M., Galli, C. L., Lonati, G., Ozgen, S., Papale, A., Signorini, S., Tardivo, R., Valli, G., and Marinovich, M.: The chemical composition of ultrafine particles and associated biological effects at an alpine town impacted by wood burning, Sci. Total Environ., 587–588, 223–231, https://doi.org/10.1016/j.scitotenv.2017.02.125, 2017.

Currie, L. A.: Nomenclature in evaluation of analytical methods including detection and quantification capabilities (IUPAC Recommendations 1995), Pure Appl. Chem., 67, 1699–1723, https://doi.org/10.1351/pac199567101699, 1995.

De Jesus, A. L., Rahman, M. M., Mazaheri, M., Thompson, H., Knibbs, L. D., Jeong, C., Evans, G., Nei, W., Ding, A., Qiao, L., Li, L., Portin, H., Niemi, J. V., Timonen, H., Luoma, K., Petäjä, T., Kulmala, M., Kowalski, M., Peters, A., Cyrys, J., Ferrero, L., Manigrasso, M., Avino, P., Buonano, G., Reche, C., Querol, X., Beddows, D., Harrison, R. M., Sowlat, M.

H., Sioutas, C., and Morawska, L.: Ultrafine particles and $PM_{2.5}$ in the air of cities around the world: Are they representative of each other?, Environ. Int., 129, 118–135, https://doi.org/10.1016/j.envint.2019.05.021, 2019.

DeCarlo, P., Slowik, J., Worsnop, D., Davidovits, P., and Jimenez, J.: Particle Morphology and Density Characterization by Combined Mobility and Aerodynamic Diameter Measurements. Part 1: Theory, Aerosol Sci. Technol., 38, 1185–1205, https://doi.org/10.1080/02786826.2004.10399461, 2004.

DeCarlo, P. F., Kimmel, J. R., Trimborn, A., Northway, M. J., Jayne, J. T., Aiken, A. C., Gonin, M., Fuhrer, K., Horvath, T., Docherty, K. S., Worsnop, D. R., and Jimenez, J. L.: Field-Deployable, High-Resolution, Time-of-Flight Aerosol Mass Spectrometer, Anal. Chem., 78, 8281–8289, https://doi.org/10.1021/ac061249n, 2006.

Donaldson, K., Stone, V., Clouter, A., Renwick, L., and MacNee, W.: Ultrafine particles, Occup. Environ. Med., 58, 211–216, https://doi.org/10.1136/oem.58.3.211, 2001.

Eeftens, M., Phuleria, H. C., Meier, R., Aguilera, I., Corradi, E., Davey, M., Ducret-Stich, R., Fierz, M., Gehrig, R., Ineichen, A., Keidel, D., Probst-Hensch, N., Ragettli, M. S., Schindler, C., Künzli, N., and Tsai, M.-Y.: Spatial and temporal variability of ultrafine particles, NO_2, $PM_{2.5}$, $PM_{2.5}$ absorbance, PM_{10} and PM_{coarse} in Swiss study areas, Atmos. Environ., 111, 60–70, https://doi.org/10.1016/j.atmosenv.2015.03.031, 2015.

Florou, K., Papanastasiou, D. K., Pikridas, M., Kaltsonoudis, C., Louvaris, E., Gkatzelis, G. I., Patoulias, D., Mihalopoulos, N., and Pandis, S. N.: The contribution of wood burning and other pollution sources to wintertime organic aerosol levels in two Greek cities, Atmospheric Chem. Phys., 17, 3145–3163, https://doi.org/10.5194/acp-17-3145-2017, 2017.

Furger, M., Minguillón, M. C., Yadav, V., Slowik, J. G., Hüglin, C., Fröhlich, R., Petterson, K., Baltensperger, U., and Prévôt, A. S. H.: Elemental composition of ambient aerosols measured with high temporal resolution using an online XRF spectrometer, Atmospheric Meas. Tech., 10, 2061–2076, https://doi.org/10.5194/amt-10-2061-2017, 2017.

Giechaskiel, B., Melas, A., Martini, G., and Dilara, P.: Overview of Vehicle Exhaust Particle Number Regulations, Processes, 9, 2216, https://doi.org/10.3390/pr9122216, 2021.

Giechaskiel, B., Melas, A., Martini, G., Dilara, P., and Ntziachristos, L.: Revisiting Total Particle Number Measurements for Vehicle Exhaust Regulations, Atmosphere, 13, 155, https://doi.org/10.3390/atmos13020155, 2022.

Gilardoni, S., Massoli, P., Giulianelli, L., Rinaldi, M., Paglione, M., Pollini, F., Lanconelli, C., Poluzzi, V., Carbone, S., Hillamo, R., Russell, L. M., Facchini, M. C., and Fuzzi, S.: Fog scavenging of organic and inorganic aerosol in the Po Valley, Atmospheric Chem. Phys., 14, 6967–6981, https://doi.org/10.5194/acp-14-6967-2014, 2014.

Halek, F., Kianpour-Rad, M., and Kavousirahim, A.: Seasonal variation in ambient PM mass and number concentrations (case study: Tehran, Iran), Environ. Monit. Assess., 169, 501–507, https://doi.org/10.1007/s10661-009-1192-2, 2010.

HEI: Review Panel on Ultrafine Particles. Understanding the Health Effects of Ambient Ultrafine Particles., Health Effects Institute, Boston ,MA, 2013.

Hinds, W. C.: Aerosol technology: Properties, behavior, and measurement of airborne particles., John Wiley and Sons, 1999.

Jalava, P. I., Salonen, R. O., Pennanen, A. S., Sillanpää, M., Hälinen, A. I., Happo, M. S., Hillamo, R., Brunekreef, B., Katsouyanni, K., Sunyer, J., and Hirvonen, M.-R.: Heterogeneities in Inflammatory and Cytotoxic Responses of RAW 264.7 Macrophage Cell Line to Urban Air Coarse, Fine, and Ultrafine Particles From Six European Sampling Campaigns, Inhal. Toxicol., 19, 213–225, https://doi.org/10.1080/08958370601067863, 2007.

Kim, J. H., Mulholland, G. W., Kukuck, S. R., and Pui, D. Y. H.: Slip correction measurements of certified PSL nanoparticles using a nanometer differential mobility analyzer (nano-DMA) for Knudsen number from 0.5 to 83, J. Res. Natl. Inst. Stand. Technol., 110, 31, https://doi.org/10.6028/jres.110.005, 2005.

Kittelson, D., Khalek, I., McDonald, J., Stevens, J., and Giannelli, R.: Particle emissions from mobile sources: Discussion of ultrafine particle emissions and definition, J. Aerosol Sci., 159, 105881, https://doi.org/10.1016/j.jaerosci.2021.105881, 2022.

Kostenidou, E., Pathak, R. K., and Pandis, S. N.: An Algorithm for the Calculation of Secondary Organic Aerosol Density Combining AMS and SMPS Data, Aerosol Sci. Technol., 41, 1002–1010, https://doi.org/10.1080/02786820701666270, 2007.

Kostenidou, E., Florou, K., Kaltsonoudis, C., Tsiflikiotou, M., Vratolis, S., Eleftheriadis, K., and Pandis, S. N.: Sources and chemical characterization of organic aerosol during the summer in the eastern Mediterranean, Atmospheric Chem. Phys., 15, 11355–11371, https://doi.org/10.5194/acp-15-11355-2015, 2015.

Kumar, P., Wiedensohler, A., Birmili, W., Quincey, P., and Hallquist, M.: Ultrafine Particles Pollution and Measurements, in: Comprehensive Analytical Chemistry, vol. 73, Elsevier, 369–390, https://doi.org/10.1016/bs.coac.2016.04.004, 2016.

Kuwayama, T., Ruehl, C. R., and Kleeman, M. J.: Daily Trends and Source Apportionment of Ultrafine Particulate Mass ($PM_{0.1}$) over an Annual Cycle in a Typical California City, Environ. Sci. Technol., 47, 13957–13966, https://doi.org/10.1021/es403235c, 2013.

Kwon, H.-S., Ryu, M. H., and Carlsten, C.: Ultrafine particles: unique physicochemical properties relevant to health and disease, Exp. Mol. Med., 52, 318–328, https://doi.org/10.1038/s12276-020-0405-1, 2020.

Lanz, V. A., Alfarra, M. R., Baltensperger, U., Buchmann, B., Hueglin, C., and Prévôt, A. S. H.: Source apportionment of submicron organic aerosols at an urban site by factor analytical modelling of aerosol mass spectra, Atmospheric Chem. Phys., 7, 1503–1522, https://doi.org/10.5194/acp-7-1503-2007, 2007.

Li, N., Sioutas, C., Cho, A., Schmitz, D., Misra, C., Sempf, J., Wang, M., Oberley, T., Froines, J., and Nel, A.: Ultrafine particulate pollutants induce oxidative stress and mitochondrial damage., Environ. Health Perspect., 111, 455–460, https://doi.org/10.1289/ehp.6000, 2003.

Majcen, N., Bettencourt da Silva, R., and Europäische Kommission (Eds.): Analytical measurement: measurement uncertainty and statistics, Publications Office of the European Union, Luxembourg, 237 pp., https://doi.org/10.2787/5825, 2012.

Marcias, G., Fostinelli, J., Catalani, S., Uras, M., Sanna, A. M., Avataneo, G., De Palma, G., Fabbri, D., Paganelli, M., Lecca, L. I., Buonanno, G., and Campagna, M.: Composition of Metallic Elements and Size Distribution of Fine and Ultrafine Particles in a Steelmaking Factory, Int. J. Environ. Res. Public. Health, 15, 1192, https://doi.org/10.3390/ijerph15061192, 2018.

Marval, J. and Tronville, P.: Ultrafine particles: A review about their health effects, presence, generation, and measurement in indoor environments, Build. Environ., 216, 108992, https://doi.org/10.1016/j.buildenv.2022.108992, 2022.

Mataras, K., Siouti, E., Patoulias, D., and Pandis, S.: Significant spatial and temporal variation of the concentrations and chemical composition of ultrafine particulate matter over Europe, EGUsphere[preprint], https://doi.org/10.5194/egusphere-2024-3357, 7 November 2024.

Moreno-Ríos, A. L., Tejeda-Benítez, L. P., and Bustillo-Lecompte, C. F.: Sources, characteristics, toxicity, and control of ultrafine particles: An overview, Geosci. Front., 13, 101147, https://doi.org/10.1016/j.gsf.2021.101147, 2022.

Nel, A., Xia, T., Mädler, L., and Li, N.: Toxic Potential of Materials at the Nanolevel, Science, 311, 622–627, https://doi.org/10.1126/science.1114397, 2006.

Ohlwein, S., Kappeler, R., Kutlar Joss, M., Künzli, N., and Hoffmann, B.: Health effects of ultrafine particles: a systematic literature review update of epidemiological evidence, Int. J. Public Health, 64, 547–559, https://doi.org/10.1007/s00038-019-01202-7, 2019.

Ostro, B., Hu, J., Goldberg, D., Reynolds, P., Hertz, A., Bernstein, L., and Kleeman, M. J.: Associations of Mortality with Long-Term Exposures to Fine and Ultrafine Particles, Species and Sources: Results from the California Teachers Study Cohort, Environ. Health Perspect., 123, 549–556, https://doi.org/10.1289/ehp.1408565, 2015.

Paatero, P.: The Multilinear Engine: A Table-Driven, Least Squares Program for Solving Multilinear Problems, including the n-Way Parallel Factor Analysis Model, J. Comput. Graph. Stat., 8, 854, https://doi.org/10.2307/1390831, 1999.

Paatero, P. and Tapper, U.: Positive matrix factorization: A non-negative factor model with optimal utilization of error estimates of data values, Environmetrics, 5, 111–126, https://doi.org/10.1002/env.3170050203, 1994.

Phairuang, W., Inerb, M., Hata, M., and Furuuchi, M.: Characteristics of trace elements bound to ambient nanoparticles ($PM_{0.1}$) and a health risk assessment in southern Thailand, J. Hazard. Mater., 425, 127986, https://doi.org/10.1016/j.jhazmat.2021.127986, 2022.

Schraufnagel, D. E.: The health effects of ultrafine particles, Exp. Mol. Med., 52, 311–317, https://doi.org/10.1038/s12276-020-0403-3, 2020.

Seinfeld, J. H. and Pandis, S. N.: Atmospheric Chemistry and Physics: From Air Pollution to Climate Change, 3rd ed., Wiley and Sons, New York, 2016.

Tavakoli, F. and Olfert, J. S.: An Instrument for the Classification of Aerosols by Particle Relaxation Time: Theoretical Models of the Aerodynamic Aerosol Classifier, Aerosol Sci. Technol., 47, 916–926, https://doi.org/10.1080/02786826.2013.802761, 2013.

Tavakoli, F. and Olfert, J. S.: Determination of particle mass, effective density, mass–mobility exponent, and dynamic shape factor using an aerodynamic aerosol classifier and a differential mobility analyzer in tandem, J. Aerosol Sci., 75, 35–42, https://doi.org/10.1016/j.jaerosci.2014.04.010, 2014.

Taylor, J. W., Allan, J. D., Liu, D., Flynn, M., Weber, R., Zhang, X., Lefer, B. L., Grossberg, N., Flynn, J., and Coe, H.: Assessment of the sensitivity of core / shell parameters derived using the single-particle soot photometer to density and refractive index, Atmospheric Meas. Tech., 8, 1701–1718, https://doi.org/10.5194/amt-8-1701-2015, 2015.

Timko, M. T., Yu, Z., Kroll, J., Jayne, J. T., Worsnop, D. R., Miake-Lye, R. C., Onasch, T. B., Liscinsky, D., Kirchstetter, T. W., Destaillats, H., Holder, A. L., Smith, J. D., and Wilson, K. R.: Sampling Artifacts from Conductive Silicone Tubing, Aerosol Sci. Technol., 43, 855–865, https://doi.org/10.1080/02786820902984811, 2009.

Tremper, A. H., Font, A., Priestman, M., Hamad, S. H., Chung, T.-C., Pribadi, A., Brown, R. J. C., Goddard, S. L., Grassineau, N., Petterson, K., Kelly, F. J., and Green, D. C.: Field and laboratory evaluation of a high time resolution x-ray fluorescence instrument for determining the elemental composition of ambient aerosols, Atmospheric Meas. Tech., 11, 3541–3557, https://doi.org/10.5194/amt-11-3541-2018, 2018.

Tronville, P., Gentile, V., and Marval, J.: Guidelines for measuring and reporting particle removal efficiency in fibrous media, Nat. Commun., 14, 5323, https://doi.org/10.1038/s41467-023-41154-4, 2023.

Ulbrich, I. M., Canagaratna, M. R., Zhang, Q., Worsnop, D. R., and Jimenez, J. L.: Interpretation of organic components from Positive Matrix Factorization of aerosol mass spectrometric data, Atmospheric Chem. Phys., 9, 2891–2918, https://doi.org/10.5194/acp-9-2891-2009, 2009.

U.S. EPA.: Integrated Science Assessment (ISA) for Particulate Matter (Final Report, Dec 2019), U.S. Environmental Protection Agency, Washington, DC, 2019.

Weichenthal, S., Bai, L., Hatzopoulou, M., Van Ryswyk, K., Kwong, J. C., Jerrett, M., Van Donkelaar, A., Martin, R. V., Burnett, R. T., Lu, H., and Chen, H.: Long-term exposure to ambient ultrafine particles and respiratory disease incidence in in Toronto, Canada: a cohort study, Environ. Health, 16, 64, https://doi.org/10.1186/s12940-017-0276-7, 2017.

Wu, Y., Liu, D., Tian, P., Sheng, J., Liu, Q., Li, R., Hu, K., Jiang, X., Li, S., Bi, K., Zhao, D., Huang, M., Ding, D., and Wang, J.: Tracing the Formation of Secondary Aerosols Influenced by Solar Radiation and Relative Humidity in Suburban Environment, J. Geophys. Res. Atmospheres, 127, e2022JD036913, https://doi.org/10.1029/2022JD036913, 2022.

Xu, W., Sun, Y., Wang, Q., Zhao, J., Wang, J., Ge, X., Xie, C., Zhou, W., Du, W., Li, J., Fu, P., Wang, Z., Worsnop, D. R., and Coe, H.: Changes in Aerosol Chemistry From 2014 to 2016

824   in Winter in Beijing: Insights From High-Resolution Aerosol Mass Spectrometry, J.
825   Geophys. Res. Atmospheres, 124, 1132–1147, https://doi.org/10.1029/2018JD029245,
826   2019.

827   Xue, W., Xue, J., Shirmohammadi, F., Sioutas, C., Lolinco, A., Hasson, A., and Kleeman, M. J.:
828   Day-of-week patterns for ultrafine particulate matter components at four sites in California,
829   Atmos. Environ., 222, 117088, https://doi.org/10.1016/j.atmosenv.2019.117088, 2020a.

830   Xue, W., Xue, J., Mousavi, A., Sioutas, C., and Kleeman, M. J.: Positive matrix factorization of
831   ultrafine particle mass ($PM_{0.1}$) at three sites in California, Sci. Total Environ., 715, 136902,
832   https://doi.org/10.1016/j.scitotenv.2020.136902, 2020b.

833   Yu, X., Venecek, M., Kumar, A., Hu, J., Tanrikulu, S., Soon, S.-T., Tran, C., Fairley, D., and
834   Kleeman, M. J.: Regional sources of airborne ultrafine particle number and mass
835   concentrations in California, Atmospheric Chem. Phys., 19, 14677–14702,
836   https://doi.org/10.5194/acp-19-14677-2019, 2019.

837   Zhang, R., Wang, G., Guo, S., Zamora, M. L., Ying, Q., Lin, Y., Wang, W., Hu, M., and Wang, Y.:
838   Formation of Urban Fine Particulate Matter, Chem. Rev., 115, 3803–3855,
839   https://doi.org/10.1021/acs.chemrev.5b00067, 2015.

840